6

Research Article

Jacob LaMountain*, Amogh Raju, Daniel Wasserman and Viktor A. Podolskiy

Anomalous reflection for highly efficient subwavelength light concentration and extraction with photonic funnels

https://doi.org/10.1515/nanoph-2024-0213 Received April 15, 2024; accepted August 18, 2024; published online September 9, 2024

Abstract: Photonic funnels, microscale conical waveguides that have been recently realized in the mid-IR spectral range with the help of an all-semiconductor designer metal material platform, are promising devices for efficient coupling of light between the nanoscales and macroscales. Previous analyses of photonic funnels have focused on structures with highly conductive claddings. Here, we analyze the performance of funnels with and without cladding, as a function of material properties, operating wavelength, and geometry. We demonstrate that bare (cladding-free) funnels enable orders-of-magnitude higher enhancement of local intensity than their clad counterparts, with virtually no loss of confinement, and relate this phenomenon to anomalous reflection of light at the anisotropic material-air interface. Intensity enhancement of the order of 25, with confinement of light to wavelength/20 scale, is demonstrated. Efficient extraction of light from nanoscale areas is predicted.

Keywords: photonic funnels; subwavelength light confinement; anomalous reflection; hyperbolic materials

1 Introduction

While light absorption and generation (by molecules, quantum dots, etc.) happens at the nanoscale, light propagation

*Corresponding author: Jacob LaMountain, Department of Physics and Applied Physics, University of Massachusetts Lowell, Lowell, MA 01854, USA, E-mail: jacob_lamountain@student.uml.edu.

https://orcid.org/0000-0001-8095-838X

Amogh Raju and Daniel Wasserman, Department of Electrical and Computer Engineering, University of Texas Austin, Austin, TX 78758, USA, E-mail: amoghbs@utexas.edu (A. Raju), dw@utexas.edu (D. Wasserman) Viktor A. Podolskiy, Department of Physics and Applied Physics, University of Massachusetts Lowell, Lowell, MA 01854, USA, E-mail: viktor_podolskiy@uml.edu

typically happens in the bulk of materials and is, therefore, strongly affected by the diffraction limit [1], [2]. The mismatch between the scale of a typical quantum emitter or absorber of light and the scale of the free space wavelength of the light emitted/absorbed becomes increasingly stark as the wavelength is increased. In the mid-infrared (mid-IR, 3-20 µm), a spectral range of significant importance for sensing, thermal imaging, and spectroscopy applications [3]-[5], the above scale mismatch is particularly drastic. Some confinement of light at mid-IR frequencies can be achieved with help of high-index dielectrics [2], or alternatively, highly doped semiconductor "designer metals" [6] that provide convenient mapping of visible-frequency plasmonics to the mid-IR domain. However, as a rule, exciting plasmonic modes requires complicated coupling schemes [7]-[11] and is, therefore, wavelength-dependent and often requires nm-precision alignment.

The existing efforts to confine mid-IR light to the nanoscale include guided modes, resonators, and (noble metal-based) antennas and arrays of such structures [12]–[18], with typical enhancement of intensity of the order of 10² for structures that provide for approximately 10-nm alignment and fabrication tolerances. The majority of existing studies, however, are focused on enhancing the local fields, with few efforts aiming to analyze extraction of light from the nanoscale. The material platform presented in this work can simultaneously address light confinement and light extraction challenges within a single funnel. Moreover, the funnel platform does not require extreme alignment or fabrication precision.

When multiple plasmonic layers are stacked and separated by dielectric spacers, the plasmonic modes supported by individual metal—dielectric interfaces couple to each other, and the optical response of the multilayer metamaterial approaches that of a homogeneous medium with extreme anisotropy of dielectric permittivity. Such materials are commonly known as hyperbolic media [19]–[31]. Hyperbolic materials are known to effectively eliminate the diffraction limit and enable deep subwavelength management of light. In particular, waveguides with hyperbolic

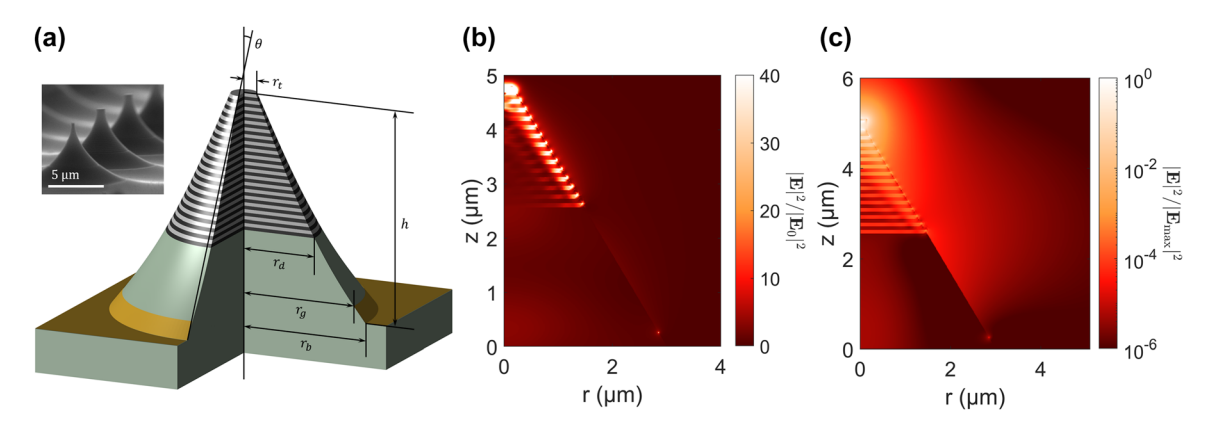


Figure 1: Hybrid photonic funnels for coupling and extraction of light to and from the nanoscale; (a) schematic representation of photonic funnels considered in this work along with relevant geometric parameters (see text for details; inset illustrates scanning electron microscopy image of the array of funnels); different shades of gray represent undoped (dielectric) and doped (plasmonic) semiconductor layers; gold colored surfaces correspond to (optional) high-conductivity claddings; (b and c) intensity distribution inside and around a photonic funnel with a dielectric base and metamaterial tip, (b) with plane waves incident through the funnel base (normalized to the field intensity above the substrate in the absence of the funnel, $|E_0|^2$) and (c) with a z-polarized dipole source at the tip of the funnel (normalized to the maximum intensity, $|E_{max}|^2$).

material cores do not exhibit mode cutoffs and support propagation of light even when the waveguide radii are much smaller than the free-space wavelength. As proposed in Ref. [32], this phenomenon can be utilized in waveguides with conical geometries, referred to as *photonic funnels*, enabling direct coupling between the nanoscale and microscale (see Figure 1). Photonic funnels have been experimentally realized in Ref. [33], demonstrating confinement of mid-IR light to wavelength/25 spatial areas. All previous studies, however, have considered funnels with highly conductive claddings and achieved relatively modest intensities at the funnel tips.

In this work we consider, in greater detail, light propagation in photonic funnels. We demonstrate that this propagation is significantly affected by the phenomenon of anomalous reflection. We compare funnels without cladding to funnels with perfect electric conductor (PEC) cladding and show that for funnels with realistic, lossy hyperbolic material cores, the cladding-free structures significantly outperform their PEC-clad counterparts. Finally, we show that efficient coupling between nanoscales and macroscales can be utilized for extracting light from the nano-domain, breaking the conventional trade-off between Purcell factor and extraction efficiency [34]–[36].

Our results, illustrated with the representative example of designer metal-based mid-IR metamaterials, can be applied to photonic funnel designs across the electromagnetic spectrum, from plasmonic noble metal-based structures at visible frequencies [25], to transparent oxide-based materials at near-IR wavelengths [26], to doped semiconductor-based media in the mid-IR, to graphene-based

hyperbolic materials operating from IR to THz frequencies [27], [28], or even homogeneous hyperbolic media [29].

1.1 Photonic funnels setup

As seen in Figure 1, a photonic funnel is a waveguide with a conical hyperbolic metamaterial (HMM) core that has a diffraction-limited base and a deep subwavelength tip. As mentioned above, photonic funnels can operate in two different modes. In the first mode, diffraction-limited light enters the funnel from the bottom of the structure and is confined within the core toward the tip. In the second mode, a (dipole) source located near the tip of the funnel emits radiation that is reshaped and routed out of the base of the funnel. An optional highly conductive cladding layer prevents the escape of guided light into the free space surrounding the funnel. Photonic funnels have the potential to have substantially larger operating frequency bandwidth than resonator-based systems [37], [38]. Separately, unlike hybrid and plasmonic waveguides [7]-[10], funnels do not require nontrivial coupling structures to convert free-space modes to surface waves.

The efficiency of light confinement can be characterized by two different figures of merit: intensity enhancement and confinement radius. For reasons of practicality, we consider funnels with dimensions and materials similar to those used in our experimental studies: InGaAs/InAlAs semiconductor structures grown lattice matched to InP. The enhancement is defined as the ratio of the intensity 50 nm above the center of the funnel tip, $|\mathbf{E}_t|^2$, to the intensity that would be observed just above the InP substrate in the absence of the funnel or HMM stack, $|\mathbf{E}_0|^2$. We define the

confinement radius $r_{\rm eff}$ of a funnel as the radial distance from the axis of the funnel to the point where the intensity, $|\mathbf{E}|^2$, falls by a factor of e^2 . As with the enhancement analysis, the confinement radius is calculated 50 nm above the funnel

The ability to couple light out from the nanoscale is quantified in terms of two metrics, the Purcell factor, F_p , and the outcoupling efficiency, $\eta_{
m out}$. The Purcell factor is defined as the ratio of the power emitted by the dipole in proximity to the funnel tip to the power emitted by an identical dipole in vacuum. The outcoupling efficiency measures the fraction of the total emitted power that is coupled to a desired channel, which is in this case diffraction-limited downward propagating light in the substrate. It is defined here as the ratio of the emitted power to the power that is transmitted down through the substrate.

1.2 Hyperbolic metamaterial cores

The dispersion of the photonic funnel cores plays a crucial role in the confinement of light to the nanoscale. Here we use, as our representative hyperbolic metamaterial, the layered InGaAs/InAlAs material platform, grown lattice matched on InP substrates [39]. In this all-semiconductor platform, the InGaAs layers are highly doped (which we denote as n^{++} doping), resulting in free-charge concentration of the order of 10¹⁹ e/cm³, which pushes the plasma frequency, ω_{p} , of the free-electron gas in the InGaAs layers to the mid-IR range. The dielectric permittivity of the doped layers of our metamaterials is well-described as a function of angular frequency, ω , by the Drude model [2]:

$$\varepsilon_m(\omega) = \varepsilon_w \left(1 - \frac{\omega_p^2}{\omega^2 + i\gamma\omega} \right)$$

with background permittivity $\varepsilon_w = 12.15$, plasma wavelength $\lambda_p = 2\pi c/\omega_p = 12.5 \,\mu\text{m}$ (where c is the speed of light in vacuum), and scattering rate $\gamma = 6.8$ THz (see Figure 2a). Note that the optical absorption of these materials is often better (lower) than what is observed for noble metals close to their respective plasma frequencies [5], [6].

When the thicknesses of the individual layers in the hyperbolic metamaterial are significantly below the freespace wavelength, the optical response of the multilayer composite closely resembles the behavior of a homogeneous medium with uniaxial anisotropy having a diagonal permittivity tensor $\hat{\varepsilon} = \{\varepsilon_{\perp}, \varepsilon_{\perp}, \varepsilon_{zz}\}$, with components

$$\varepsilon_{\perp} = \frac{\varepsilon_m + \varepsilon_d}{2}, \varepsilon_{zz} = \frac{2\varepsilon_m \varepsilon_d}{\varepsilon_m + \varepsilon_d}$$

with $\varepsilon_d = 10.23$ being the permittivity of the undoped InAlAs layers. These expressions assume identical thicknesses d for the InGaAs and InAlAs layers, a condition that is typically realized in experiments. We use d = 80 nm in this work. Note that the layer thicknesses are much smaller than the vacuum wavelength, $d \ll \lambda_0$. Figure 2b illustrates the wavelength-dependence of the components of the permittivity tensor for the metamaterial. The same figure also illustrates three main frequency ranges where the composite behaves as anisotropic dielectric, and as type-I or type-II hyperbolic material Section 2 of the Supplementary Material additional discussion about the validity of effective medium theory.

1.3 Anomalous reflections at planar interfaces

The direction of reflected and refracted beams at a planar interface between two materials can be related to the dispersion of the waves supported by these media. It is wellknown that an interface between hyperbolic and isotropic materials supports negative (phase or group) refraction

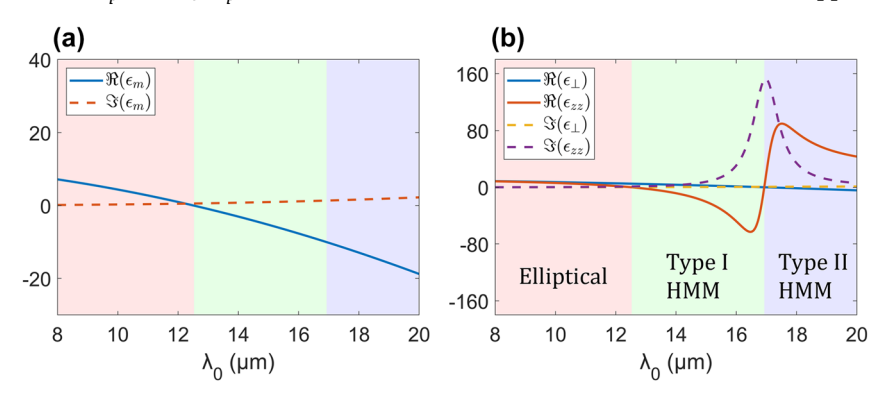


Figure 2: Spectral response of materials; (a) permittivity of doped plasmonic layers and (b) effective permittivity of the all-semiconductor multilayer metamaterial; background colors illustrate frequency ranges corresponding to different optical topologies of the metamaterial response with (red) elliptic, (green) type I hyperbolic and (purple) type II hyperbolic regimes [25], [40].

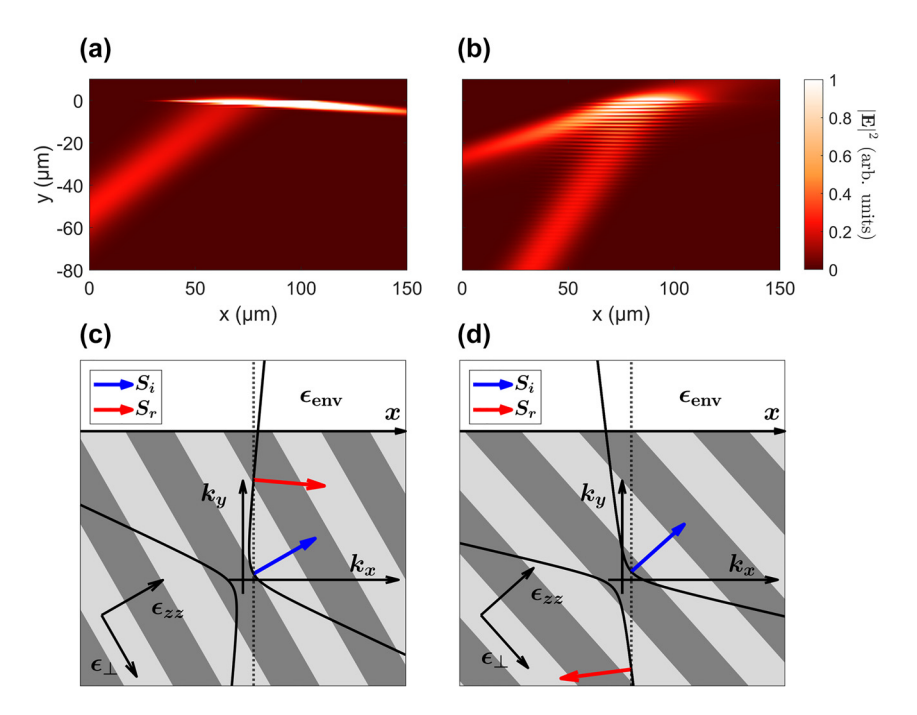


Figure 3: Anomalous reflections; (a, b) 2D simulation of an anomalous reflection of a Gaussian-shaped beam at the interface between a hyperbolic metamaterial (based on $\varepsilon_m = -2 + 0.01i$, $\varepsilon_d = 10.23$, d = 80 nm, $\lambda_0 = 13.5$ µm; see Section 2 of the Supplementary Material for a discussion on the validity of effective medium theory) and vacuum. Panels (a, b) show intensity distributions in the regime of (a) positive and (b) negative anomalous reflection; panels (c. d) illustrate these regimes from the standpoint of conservation of the wavevector component parallel to the interface. The figures show dispersion of composites in the regime of (c) positive and (d) negative reflection; in all cases, the incident beam propagates along the optical axis; arrows represent directions of the (blue) incoming and (red) reflected beams; note that the energy flux is normal to the isofrequency dispersion.

[40], [41]. When the optical axis of the hyperbolic material is oblique to the interface, reflection is significantly affected as well. In these situations, conservation of the in-plane component of the wavevector requires that the angle of reflection of transverse magnetic (TM) polarized light is different from its angle of incidence [42], [43]. This phenomenon, often referred to as anomalous reflection, is illustrated in Figure 3. Anomalous reflection is particularly interesting when the angle between the optical axis and the interface is close to the critical angle [44] of the hyperbolic material

$$\tan \theta_c \simeq \sqrt{-\varepsilon_\perp'/\varepsilon_{zz}'}$$

In these situations, the reflected beam is significantly compressed, and the electric field in the reflected beam is enhanced with respect to that in the incident beam (such enhancement can be related to the ε near zero condition in the reference frame coaligned with the reflected beam). Notably, both positive and negative reflection of light is possible, depending on the relationship between the optical axis and the direction of the interface. Here we are interested in the situation where the incoming beam is

coaligned with the optical axis, in which case the strongly collimated anomalously reflected beam resembles a surface mode propagating along the interface between the hyperbolic and isotropic media.

2 Results

Below we describe our analysis of coupling light to and from the nanoscale and present results of our experimental studies of fabricated dielectric, hyperbolic, and hybrid photonic funnels. In the initial studies reported below, we fix the input and output radius of the funnels to $r_b = 3 \, \mu \text{m}$ and $r_t = 150$ nm, respectively. The gold radius, r_g , was set to 95 % of the base radius for clad-less and 105 % of the tip radius for PEC clad funnels. To assess the impact of shape variation, we consider funnels of differing height with linear dependence of radius on coordinate (effectively changing the "speed" of light confinement). Funnels with and without PEC cladding are analyzed. Scanning electron microscope (SEM) analysis is used to inform our simulations of experimentally realized funnels.

2.1 Efficient confinement of light to the nanoscale

As mentioned above, the performance of the photonic funnels is characterized via two figures of merit, intensity enhancement at the tip of the funnel and confinement radius. For the optimal funnels, intensity enhancement should be maximized while confinement radius should be minimized.

Figure 4 summarizes our analysis. The behavior of photonic funnels with anisotropic cores critically depends on whether the funnel includes a metallic cladding. At lower wavelengths, where the multilayer metamaterial behaves as an "elliptic" transparent uniaxial medium ($\varepsilon_{\perp}>\varepsilon_{zz}>$ 0), the performance of the funnels is very close to that of conventional dielectric waveguides [2]; light confinement is present only in relatively tall PEC-clad structures and is never accompanied by intensity enhancement. Notably, the amount of light reaching the nanoscale tips of metal-clad funnels is exponentially suppressed as a function of funnel height - a direct manifestation of the diffraction limit.

At the same time, when the optical response of the core moves into the type-I hyperbolic range, and when – as a result - the diffraction limit ceases to exist within the funnel, the hyperbolic funnels provide significantly better confinement – and significantly higher intensities at the tips of the funnel - than their isotropic counterparts. Note that this phenomenon extends throughout the type-I hyperbolicity frequency range.

However, when intensity at the tip is compared to the intensity of diffraction-limited light above the bare substrate, it becomes evident that material absorption in the funnels with conductive cladding significantly restricts the benefits of hyperbolic dispersion. The losses associated with the hyperbolic response ensure that the intensity of the highly confined light at the funnel tip is no higher than the intensity of light that would be observed above a bare, lossless substrate (in the absence of any confinement). Interestingly, the optimal geometry of the metal-clad funnel depends on operating wavelength, with maximum performance achieved when the funnel angle is close to the critical angle of the metamaterial (green dashed line in Figure 4).

The situation changes drastically when the conductive cladding is eliminated. Here, intensity at the tip of the (lossy) funnel reaches almost an order of magnitude higher than the intensity of light in the absence of the funnels. In other words, the clad-less funnel provides highly efficient confinement of electromagnetic energy. Once again, the region of

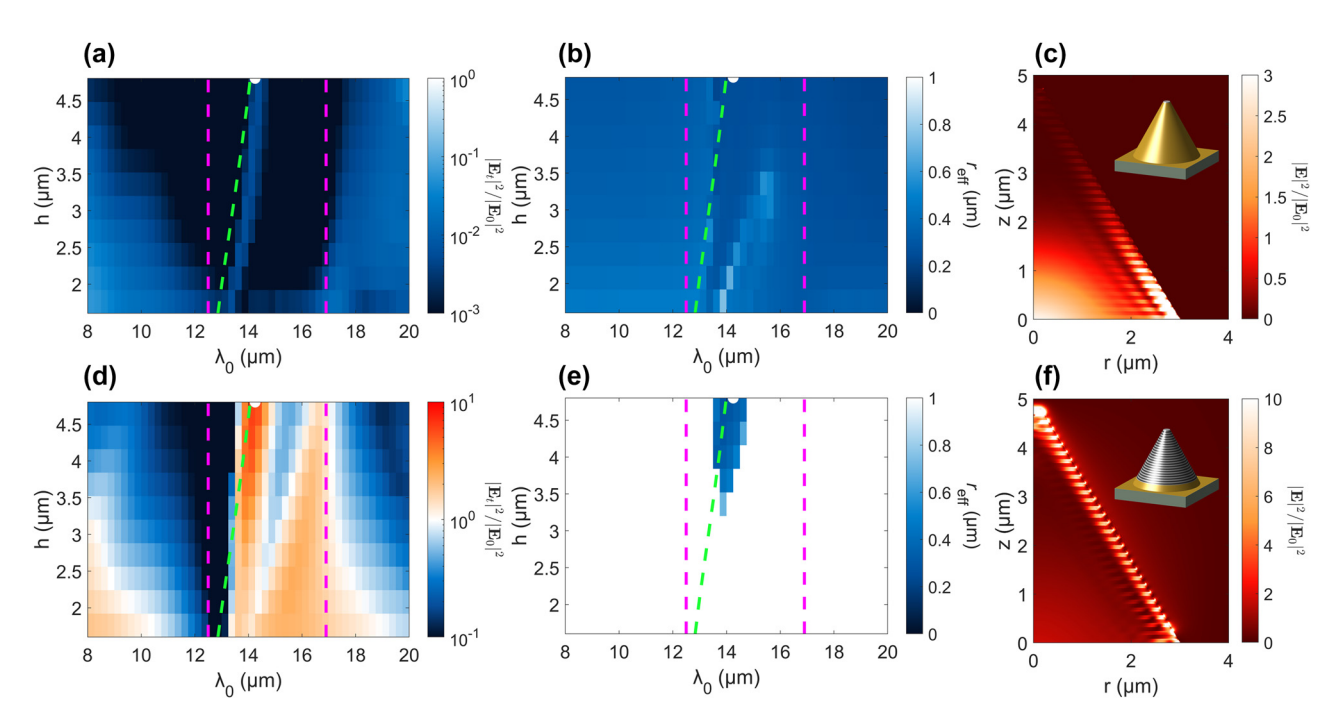


Figure 4: Light concentration in photonic funnels; (a, d) tip intensity enhancement and (b, e) confinement radius in funnels with metamaterial cores having a linear sidewall profile (a...c) with and (d...f) without PEC claddings; green dashed lines in (a, d) correspond to the condition when the funnel angle θ is equal to the critical angle θ_c ; magenta lines represent the wavelengths of topological transitions in the metamaterial's response. Panels (c, f) illustrate intensity distributions within and around the funnels for geometry/wavelength combinations denoted by solid white spots in (a, d), respectively; white areas in (e) represent conditions where the funnel does not provide subwavelength confinement ($r_{eff} > 1 \mu m$).

maximum performance closely follows the condition when the funnel opening matches the critical angle of the metamaterial. It is important to note that clad-less funnels provide both enhancement and strong confinement of light in this region of the parameter space.

To gain understanding into the origin of the differences between the structures with and without cladding, we analyzed the field distributions of an exemplary funnel of each type at the wavelength of their greatest tip intensity. These distributions are shown in Figure 4(c) and (f). It is seen that in both situations, light scattering (reflection) at the oblique interface yields excitation of the beams that propagate in the direction of the critical cone in direct analogy to the anomalous reflection shown in Figure 3a (see Section 2 of the Supplementary Material for further discussion). However, the attenuation of light within the metal-clad funnel (Figure 4c) happens significantly faster than in the air-clad counterpart (Figure 4f).

Mathematically, at every z location (locally fixed radius), the distribution of light within the funnels can be represented as a linear combination of guided modes and (in the case of clad-less structures) a spectrum of leaky modes [45]. Spatial change of the radius leads to (i) modification of the field distributions and propagation constants of the modes and to (ii) redistribution of light between different modes. Our analysis of the properties of the guided modes that are responsible for confining radiation toward the nanoscale tip (Table 1) clearly shows that modes in the PEC-clad funnels have significantly higher propagation losses than modes in cladding-free structures.

Importantly, in both scenarios, the decrease of the radius yields an increase of the effective index, reflecting the hyperbolicity-induced postponement of the diffraction limit. As a result, the semiclassical regime that is responsible for the formation of the critical cone-like beams that originate from anomalous reflections at the funnel interfaces is

Table 1: Effective indices $(n_z=k_zc/\omega)$ of lowest-propagation loss TM-like guided modes in circular cylindrical waveguides with hyperbolic cores with $\varepsilon_\perp=3.6+0.4i$, $\varepsilon_{zz}=-8.4+3.1i$, representing an HMM at $\lambda_0=14~\mu\mathrm{m}$ with PEC and air claddings; in all calculations, the axial mode number m=1.

Radius (um)	$n_{\rm z}$ in PEC-clad guides	n _z in air-clad guides
3	2.6 + 0.4 <i>i</i>	2.0 + 0.2i
2	3.3 + 0.6i	2.3 + 0.3i
1	5.6 + 1.2 <i>i</i>	3.5 + 0.7i
0.5	10.8 + 2.5i	6.3 + 1.4 <i>i</i>
0.1	52.9 + 12.4 <i>i</i>	30.4 + 7.3i

sustained throughout the funnel and is not limited to the funnel base.

2.2 Efficient outcoupling of light from the nanoscale

We now consider perspectives of using photonic funnels for efficient extraction of light from the nanoscale. Environment-induced modulation of emission can be split into two related but separate effects: (i) the Purcell effect, which enhances the probability of emission, measured by the Purcell factor F_p , and (ii) emission re-shaping, a group of processes responsible for outcoupling the radiation into the far field, measured here by outcoupling efficiency η_{out} . Hyperbolic materials (as well as plasmonic- and phononicmedia in general) provide significant Purcell factors by introducing plasmon- (phonon-) related decay channels [34]. Unfortunately, a vast majority of plasmonic modes do not easily couple to free-space radiation. As a result, there is often a trade-off between high Purcell factor and high outcoupling efficiency [34]-[36]. Photonic funnels can alleviate this trade-off.

Funnel-induced emission modulation is summarized in Figure 5. Similar to what has been predicted theoretically and demonstrated in experiments with planar hyperbolic composites [46], photonic funnels provide significant enhancement of the Purcell effect when the core operates in the hyperbolic regime. However, in contrast to what has been demonstrated in planar structures, the high Purcell factors in photonic funnels often coincide with the regime of efficient light extraction - both have maxima at wavelengths for which the funnel angle is close to the critical angle. This effect is a time-reversal counterpart of the efficient confinement discussed above. Indeed, the photonic density of states in hyperbolic metamaterials is dominated by the modes propagating along the critical cones [41]. Anomalous reflection allows for direct coupling between these modes and diffraction-limited light propagating along the optical axis of the metamaterial (axis of the funnel). Notably, there exists a spectral shift in the emission of in-plane and z-oriented dipoles, originating from the variation between emission profiles of dipoles of different orientation.

Analysis of emission spectra reveals a second peak in outcoupling efficiency at $\lambda_0 \sim$ 17 μm . This peak is associated with direct conversion of light emitted along the critical cone to propagating light by refracting at the funnel–substrate interface. For tall funnels, this phenomenon converges to beaming in the z direction in the epsilon near zero (ENZ, $\varepsilon_\perp \simeq$ 0) regime.

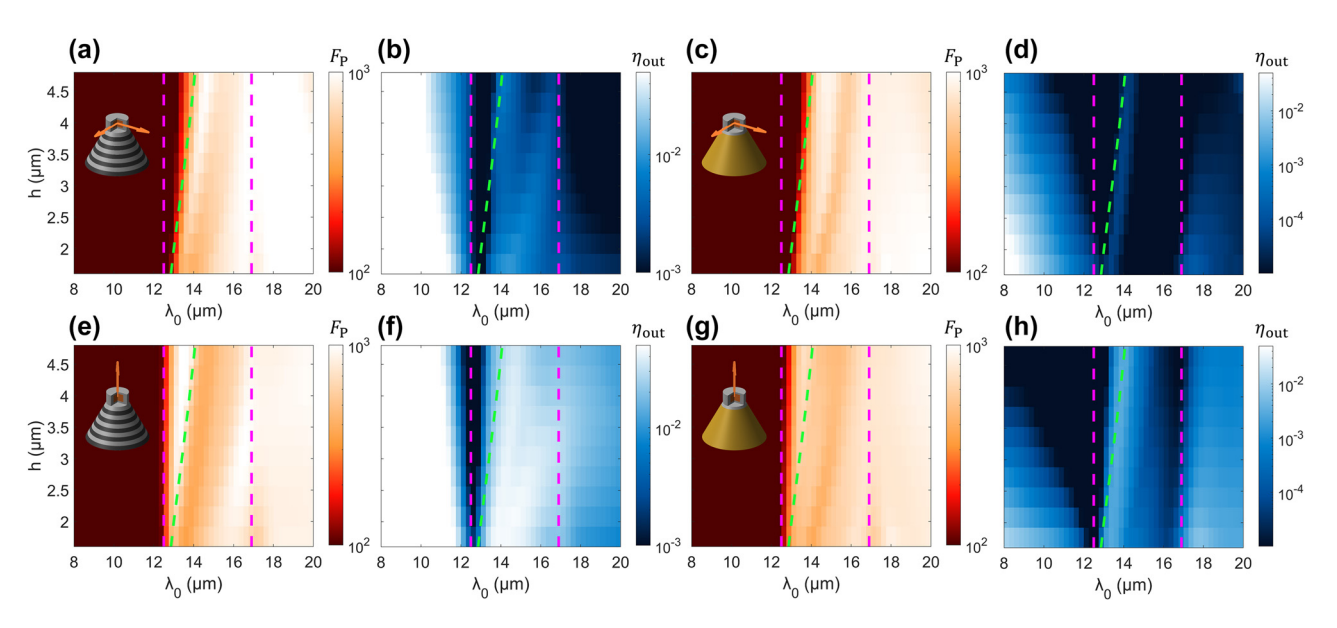


Figure 5: Light extraction in photonic funnels; (a, c, e, g) purcell factors and (b, d, f, h) outcoupling efficiencies of (a...d) in-plane and (e...h) z-polarized dipoles radiating near the tip of (a, b, e, f) air-clad and (c, d, q, h) PEC-clad funnels; green and magenta dashed lines correspond to the condition when the funnel angle θ is equal to the critical angle θ_r and to topological transitions in the metamaterial's response, respectively.

2.3 Further optimization considerations

Since the hyperbolic dispersion of the composites used in this study originates from the plasmonic response of the highly doped components of the metamaterials, optical loss associated with this response serves as a significant limiting factor in the performance of the metamaterial-based structures. This point is illustrated in Figure 6(a)–(c), which show the predicted performance of funnels that have half of the plasmonic loss observed in experiments, providing for an additional factor of ~10 in intensity enhancement at the tip.

Given that plasmonic absorption in practical materials is difficult to control, it is beneficial to look for solutions outside loss reduction. Dielectric waveguides can confine light up to the point of the diffraction limit with propagation and confinement of light only limited by reflection, not absorption loss. Therefore, hybrid funnels that have a dielectric core at their diffraction-limited base and switch to hyperbolic cores close to their tip may provide a significant boost in the funnels' performance. Importantly, such hybrid funnels can be relatively straightforwardly fabricated using molecular beam epitaxy (MBE) growth and the chemical etch techniques reported in our previous work [33], with the chemical etch for the hybrid funnels extending into the semiconductor substrate – beyond the multilayer part of the funnels.

In our numerical studies, the shape of the hybrid funnels was identical to that of the funnels with multilayer cores (reported above). We assumed that the inside of each

structure is filled with isotropic material (with permittivity identical to that of the substrate) up until the radius of the funnel reaches $r_d = 1.5 \, \mu \text{m}$, with the thinner "tip" of the funnel comprising multilayered material.

Performance of such hybrid funnels is shown in Figure 6(d)-(f). It is seen that intensity enhancement in such hybrid structures is \sim 5 times higher than that achieved in their fully plasmonic counterparts, with performance gain due to the hybrid design roughly half of what would be achievable with half-loss structures. Dipole emission studies of these same hybrid funnels show an outcoupling efficiency of about twice that of the HMM-core funnels with minimal impact on their Purcell factors.

2.4 Experimental realization of clad-less and hybrid photonic funnels

To illustrate the feasibility of light confinement to the nanoscale, we experimentally realized photonic funnel structures operating in the mid-IR frequency range. The geometry of the structures is shown in Figure 7 (details of sample fabrication are given in Section 4). Given that near-field optical microscopy at mid-IR frequencies is challenging, particularly for structures with such dramatic topographic profiles, we limit the experimental optical analysis of the structures to far-field transmission spectra and only analyze the predicted near-field confinement with full wave numerical solutions of Maxwell equation. It is seen that overall, the simulated and experimentally observed spectra

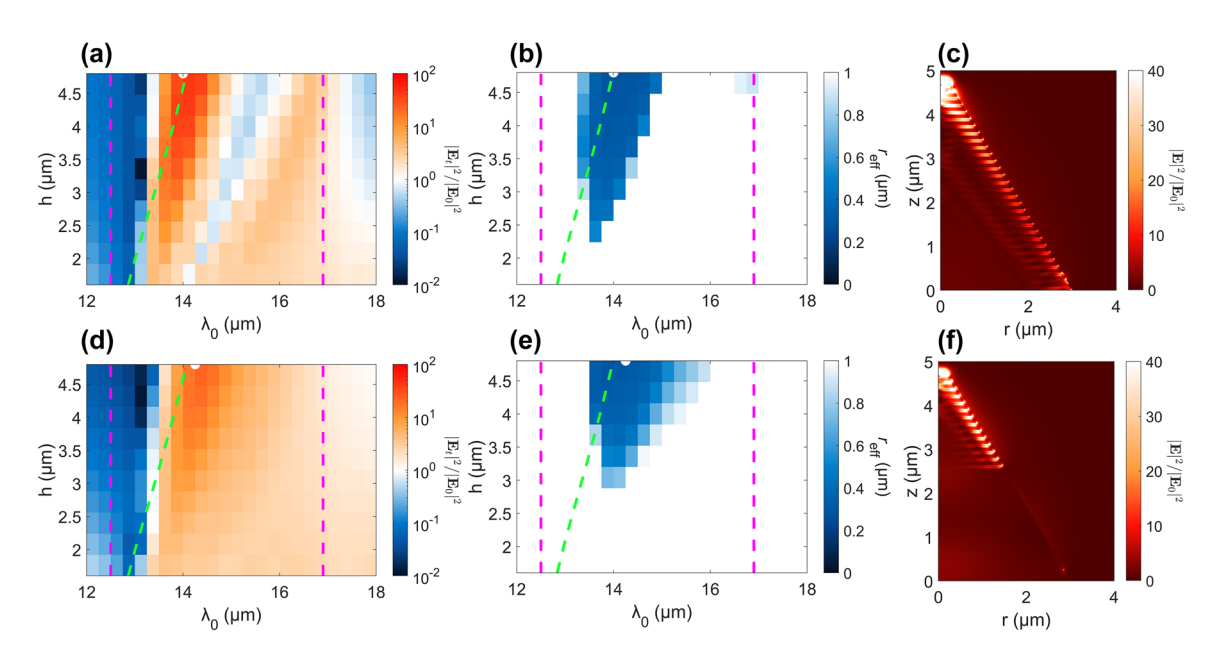


Figure 6: Light concentration in low loss and hybrid photonic funnels; (a, d) intensity enhancement, (b, e) confinement radius, and (c, f) intensity distributions in (a...c) air-clad funnels with half-loss and (d...f) in hybrid (full loss) funnels; dashed lines are identical to those in Figures 4 and 5.

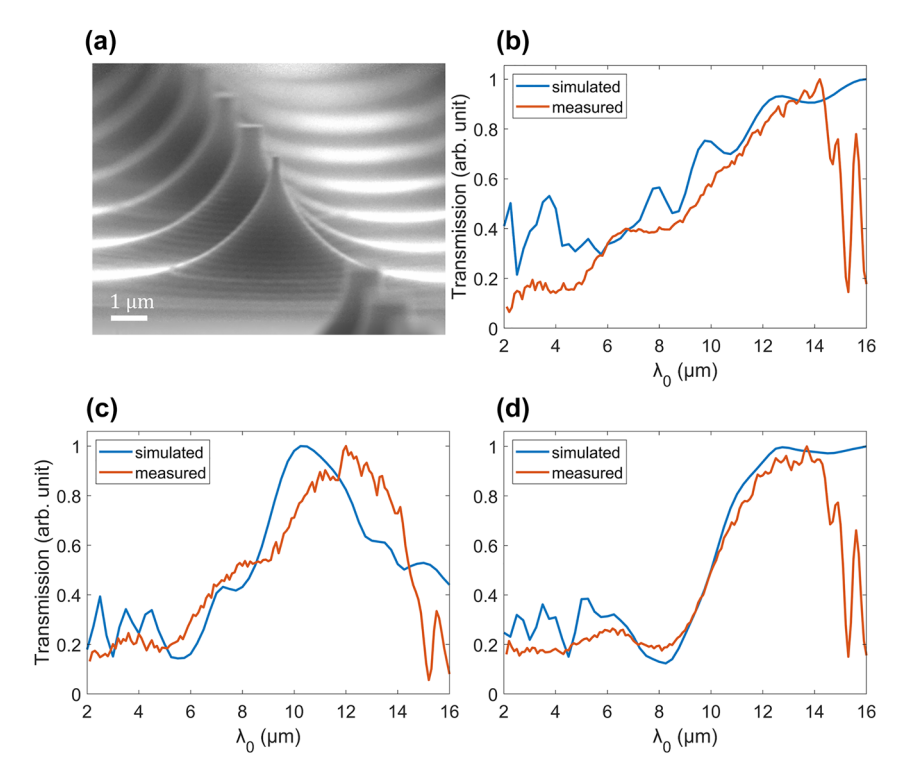


Figure 7: Experimental studies of photonic funnels; (a) SEM image of the array of photonic funnels without PEC claddings; panels (b...d) show simulated (blue lines) and experimentally observed (orange lines) transmission through individual funnels with (b) dielectric, (c) hyperbolic, and (d) hybrid cores.

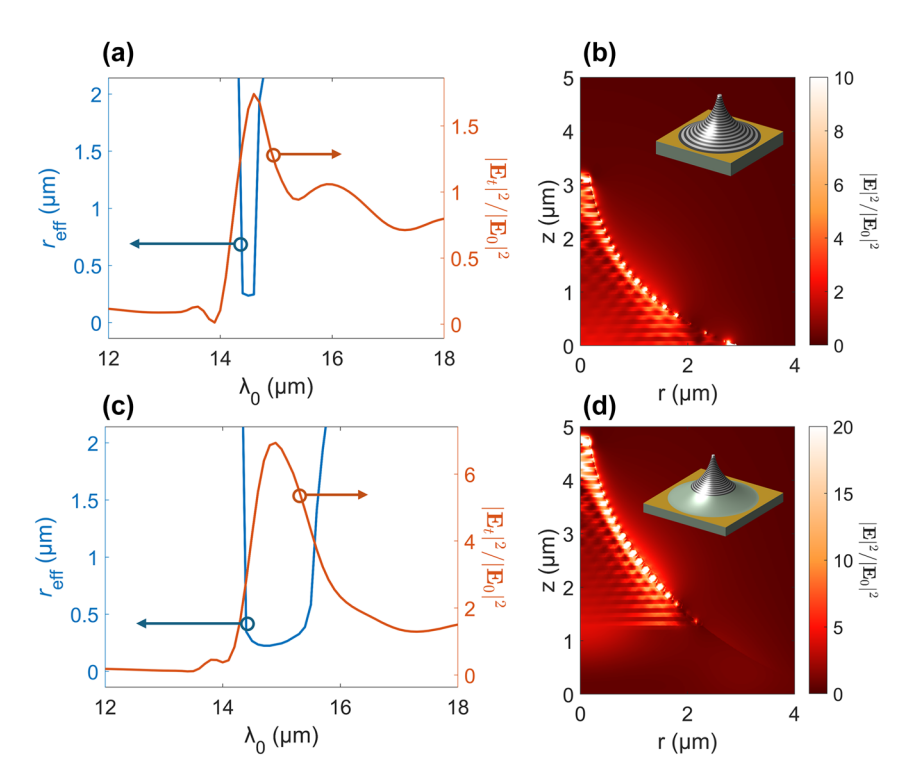


Figure 8: Simulated near-field performance of experimentally realized funnels, characterized by [left axes in (a, c)] confinement radius ref and [right axes in (a, c)] tip intensity enhancement of (a, b) hyperbolic and (c, d) hybrid funnels; panels (b, d) illustrate distribution of electric field for optimal conditions of the funnels with insets showing funnel geometries.

strongly agree with each other. The strong long-wavelength $(\lambda_0 > 14 \,\mu\text{m})$ absorption features observed in the experimental plots are related to absorption in the InP substrate. The remaining discrepancies between numerical and experimental spectra likely originate from the differences between the relatively complex experimental geometry and simpler numerical model that assumes normally incident light (see Methods). Further, the narrow resonances at short wavelengths are particularly sensitive to funnel geometry (see Figure 7a and Section 3 of the Supplementary Material).

The strong agreement between far field spectra obtained in experiments and in theoretical studies allows us to analyze the predicted field confinement in realistic funnels. Figure 8 illustrates the predicted near-field performance of these structures, demonstrating efficient confinement of light to the nanoscale. Both realistic HMM and hybrid core funnels show simultaneous enhancement and confinement of light to wavelength/30 areas, with hybrid funnels achieving a greater than 6 times intensity enhancement. While this enhancement is smaller than the one predicted in Figure 6, we note that funnels in our experiments have not been optimized. Adjusting the number of layers, doping, as well as height of the resulting structure will bring the performance of actual funnels in

line with theoretical predictions. Realizing these optimized structures is among the topics for future studies.

3 Conclusion and discussion

To conclude, we analyzed the effects of the geometry of photonic funnels with multilayer metamaterial cores on light confinement and light extraction in these structures. We demonstrated that hyperbolic dispersion enables significant (of the order of wavelength/20) confinement of light, combined with strong (×25) enhancement of local intensity. We related the light concentration at the tip of the funnels to anomalous reflection of light at the core/cladding interface. Reduction of material absorption – by either using lossless dielectric media in the diffraction-limited base of the funnel or by mitigating ohmic losses within the plasmonic media – may yield even higher intensities and more broadband performance.

All-semiconductor photonic funnels capable of efficiently confining mid-IR light to the nanoscale have been demonstrated in experiment. Their far-field performance has been validated experimentally, while their near-field properties have been analyzed numerically.

Finally, we demonstrated efficient extraction of light from the nanoscale that is accompanied by high Purcell factors.

Material granularity, in addition to material absorption, emerges as the ultimate factor that limits the confinement of light in multilayer-based devices. The emergence of spatial dispersion (or, equivalently, deviation from the quasistatic effective medium due to interference-related phenomena) prevents confinement of light to areas that are substantially smaller than a period of the structure [47]. At the same time, reducing the thickness of the plasmonic layers beyond the scale of the mean free path of the free electron yields deviations of permittivity of plasmonic layers from the Drude description due to the ballistic response [48]. Overall, we estimate that for funnels operating on designer metal materials, the minimum achievable confinement radius is of the order of few hundred nanometers, the scale that is demonstrated in this work.

Results of this work, presented on the example of a mid-IR all-semiconductor metamaterial platform, can be utilized to design photonic funnels operating throughout electromagnetic spectrum, from UV to THz frequencies.

4 Methods

4.1 Finite element studies

Numerical analysis presented in this work is performed with the help of the commercial finite-element-method partial differential equation solver COMSOL 6.0 [49]. To optimize computational resources, we utilize the COMSOL 2D axisymmetric mode (in which all fields are proportional to $e^{-im\phi}$, with ϕ the azimuthal angle and m the angular symmetry parameter) in our frequency domain studies. In the light confinement studies, we set the angular symmetry parameter m = -1 to enable analysis of funnels excited by plane waves with circular polarization (see Section 1 of the Supplementary Material for an analysis of a funnel's response to linearly polarized light). To avoid artifacts, the simulation space is surrounded by perfectly matched layers, which are bounded by scattering boundary conditions. The funnel's cores are represented as sets of discrete layers to properly account for the effects of material granularity and for deviations from the predictions of local effective medium theory caused by such granularity [47]. The substrate, superstrate, and undoped "dielectric" layers are given constant permittivities while the "metal" layers use the wavelength-dependent Drude model permittivity, as described in the main manuscript. The gold cladding of the funnels is modeled as a perfect electric conductor on the surface of the substrate and side of the funnel.

When analyzing performance of realistic funnels (Figures 7 and 8), SEMs of the funnels used in experiments were used to parameterize the shape of the funnels in numerical studies. In all studies, $r_t=150$ nm and the surface was modeled as a quadratic Bezier curve with the central control point at radius b_r and height b_z . The hyperbolic funnel was modeled as having 20 bilayers, $r_b=2.9~\mu\text{m},\,b_r=0.5~\mu\text{m},\,\text{and}\,b_z=0.9~\mu\text{m}$. The hybrid funnel was modeled as having 23 bilayers on top of a 1.12 μ m dielectric region, $r_b=4.6~\mu\text{m},\,b_r=0.7~\mu\text{m},\,\text{and}\,b_z=1.5~\mu\text{m}$. The dielectric funnel was modeled as having a height of 2.4 μ m, $r_b=2.4~\mu\text{m},\,b_r=0.23~\mu\text{m}$, and $b_z=0.58~\mu\text{m}$. These hyperbolic and hybrid models were also used for the performance analysis as shown in Figure 8.

To evaluate the transmission through the funnel, for comparison with experimentally realized funnels, a surface integral of the *z*-component of the Poynting flux is calculated near the top boundary of the simulation space.

Meshing is set to have maximum element sizes of at most $\lambda_0/10$ in superstrate (air), $\lambda_0/38$ in substrate, $\lambda_0/50$ within the funnel, and $\lambda_0/1$, 600 in a small region above the funnel tip to reduce the effects of near-axis artifacts.

For the emission analysis, a dielectric structure with radius equal to the funnel tip radius and height of 300 nm is added to the funnel tip. Centered within this structure is an active region with a radius of 90 nm and height of 200 nm. Within the active region, there is either a cylindrically or z-polarized current serving as the source of emission (in the latter case the angular symmetry parameter is set to m=0). For the Purcell factor and outcoupling efficiencies, the total emitted power is calculated as the volume integral of Re[$\mathbf{I} \cdot \mathbf{E}^*$], where \mathbf{I} is the current density. To get the reference power for the Purcell factor, a simulation with the dipole surrounded by only vacuum is run; Purcell factor F_p is defined as the ratio between total emitted power in the presence of the funnel and in vacuum. For the outcoupling efficiency η_{out} , the downward power is calculated as the surface integral of the z-component of the Poynting flux through the bottom boundary of the simulation space; $\eta_{
m out}$ is a ratio of this outgoing Poynting flux and the total power emitted by the dipole. These procedures are consistent with previous studies of emission in planar structures [35]. Note that both $F_{\rm P}$ and $\eta_{\rm out}$ depend on dipole orientation. Performance of randomly oriented dipoles can be estimated by averaging the parameters over dipole orientation.

Matlab-COMSOL livelink is used to dynamically change the funnel geometry and material properties, as well as to efficiently postprocess the results of the FEM simulations. A sample model and the associated Matlab script are available on Github [50].

4.2 Sample fabrication

The InGaAs/InAlAs HMM stack was grown lattice matched to a semi-insulating (100) InP substrate by MBE in a Varian Gen II system with effusion sources for gallium, indium, aluminum, and silicon and with valved cracker sources for arsenic and antimony. The HMM consists of 25 alternating layers of n^{++} doped InGaAs (the optical metal) and undoped InAlAs (the dielectric) of equal thickness (80 nm). The reflection spectra of the as-grown HMM samples were measured and modeled using a multilayer transfer matrix method, treating the InAlAs and InGaAs as alternating dielectric and Drude metal layers with plasma frequency ω_n , and scattering rate γ as the fitting parameters [33].

To fabricate the funnels, a layer of SiN_x is first deposited onto the as-grown HMM sample using plasma-enhanced chemical vapor deposition. The SiN_x is then patterned into 10 × 10 disc arrays using electron-beam lithography and reactive ion etching. The patterned SiN_x serves as a hard mask for the subsequent wet etch process. Each SiN_x disc array has a different disc diameter ranging between 5 and $7 \,\mu m$ with a pitch of $10 \,\mu m$ for the InP-based dielectric and the pure HMM funnels, and diameters between 10 and 12 μ m with a pitch of 15 μ m for the hybrid funnels. The patterned sample is then wet-etched in a solution of HBr:HNO3:H2O (volumetric ratio 1:1:10) to a depth of \sim 4 µm for the InP-based dielectric and the pure HMM funnels, and \sim 6 μ m for the hybrid funnels (in our studies, etching rate was 0.88 um/min for hyperbolic funnels and approximately 0.52 um/min for hybrid funnels, accounting for difference of etching speed between metamaterials and InP substrate). The isotropic nature of the wet etch results in an undercut of the SiN_x disc hard masks, resulting in the funnel shape as seen in the SEM image of Figure 7. Both the HMM stack and the InP substrate etch similarly for the wet etch employed, leading to the smooth sidewall profile observed in the hybrid structures, with minimal change in sidewall angle at the HMM/InP interface. The above fabrication process results in funnels with top diameters as small as ~200 nm for the three dielectric, HMM, and hybrid funnels. Following the wet etch, a buffered oxide etch is used to remove the top SiN_x caps, leaving the funnels exposed for characterization.

4.3 Sample characterization

The funnels were characterized using a mid-IR microscope coupled to a Fourier transform infrared (FTIR) spectrometer. The internal blackbody globar of the FTIR was used as the IR light source in order to measure a broadband infrared response. As shown in Figure 9, the IR beam from the FTIR was focused on the backside of the arrays, through the substrate via a microscope condenser. The transmitted signal was then collected through a Cassegrain objective lens with collection angles between 15° and 30°, above the funnel array. Transmitted light was measured with a

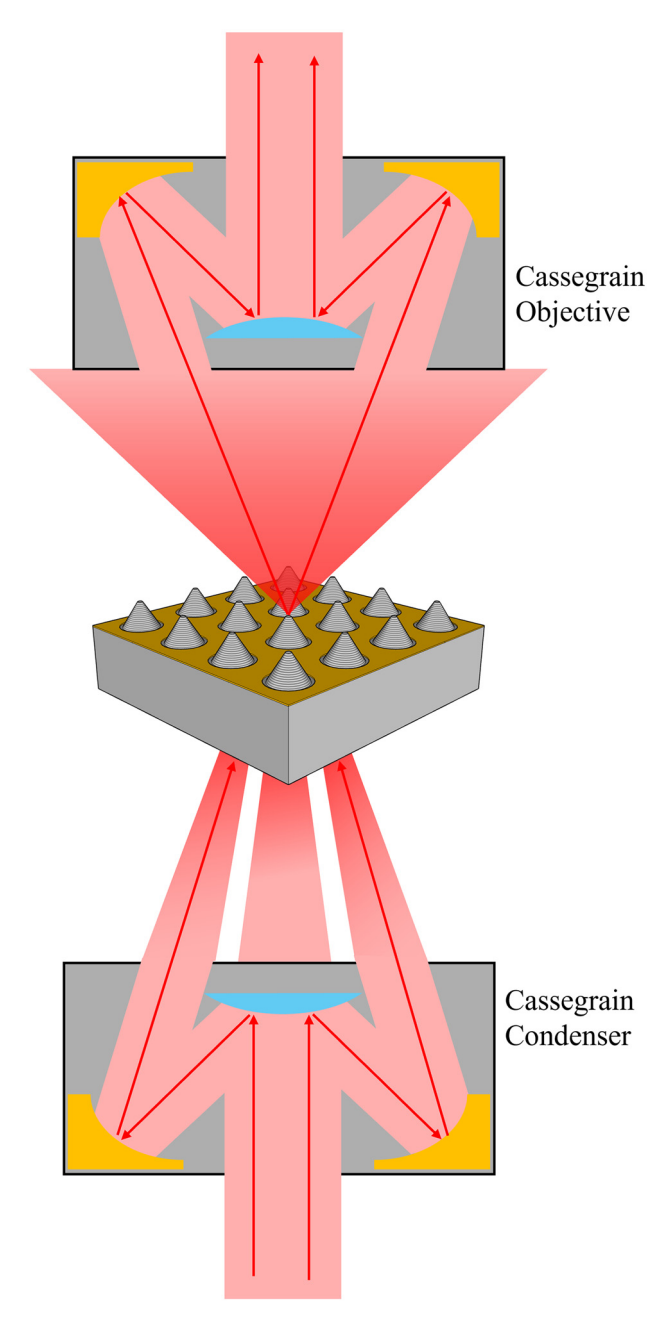


Figure 9: Schematic of experimental setup; light is focused through the substrate onto the back of a funnel with a microscope condenser and then collected with a Cassegrain objective.

liquid-nitrogen-cooled HgCdTe (MCT) detector. Transmission spectra were normalized to transmission spectra taken without the sample in place (through air). Due to the intrinsic funnel-to-funnel variation in the wet etching of the funnels, a nonuniform distribution of the funnel top diameters was obtained even within an array using etch mask discs of the same diameter. For this reason, we measure transmitted light through single funnels by aperturing the transmitted light in the image plane of the microscope. Aperture imaging areas of 10 μ m \times 10 μ m for the dielectric and HMM funnels and areas of 15 μ m \times 15 μ m for the hybrid funnels were used (accounting for the larger base diameter of the hybrid funnels). These same apertures were used for the transmission scans used to normalize transmission data for the three different funnels.

Research funding: Authors acknowledge support from the National Science Foundation, grant ## DMR-2004298 (VP) and DMR-2004422 (DW).

Author contributions: All authors have accepted responsibility for the entire content of this manuscript and approved its submission.

Conflict of interest: Authors state no conflicts of interest. **Ethical approval:** The conducted research is not related to either human or animals use.

Data availability: The datasets generated and/or analyzed during the current study are available from the corresponding author upon reasonable request.

References

- [1] F. Keilmann and R. Hillenbrand, Nano-Optics and Near-Field Optical Microscopy, A. Zayats and D. Richards, Eds., Norwood, MA, Allen House, 2009.
- [2] L. D. Landau, E. M. Lifshitz, and L. P. Pitaevskii, Electrodynamics of Continuous Media, 2nd ed. Amsterdam, Elsevier, 1984.
- [3] J. A. Sobrino, F. D. Frate, M. Drusch, J. C. Jimenez-Munoz, P. Manunta, and A. Regan, "Review of thermal infrared applications and requirements for future high-resolution sensors," IEEE Trans. Geosci. Rem. Sens., vol. 54, no. 5, p. 2963, 2016.
- [4] F. M. Hoffman, "Infrared reflection-absorption spectroscopy of adsorbed molecules," Surf. Sci. Rep., vol. 3, no. 2, p. 107, 1983.
- [5] S. Law, V. A. Podolskiy, and D. Wasserman, "Towards nano-scale photonics with micro-scale photons: the opportunities and challenges of mid-infrared plasmonics," Nanophotonics, vol. 2, no. 2, p. 103, 2013.
- [6] S. Law, D. C. Adams, A. M. Taylor, and D. Wasserman, "Mid-infrared designer metals," Opt. Express, vol. 20, no. 11, p. 12155, 2012.
- [7] S. Bozhevolnyi, V. Volov, and K. Leosson, "Localization and waveguiding of surface plasmon polaritons in random nanostructures," Phys. Rev. Lett., vol. 89, no. 18, p. 186801, 2002.

- [8] M. Stockman, "Nanofocusing of optical energy in tapered plasmonic waveguides," Phys. Rev. Lett., vol. 93, no. 13, p. 137404,
- [9] C. Ropers, C. C. Neascu, T. Elsaesser, M. Albrecht, M. B. Raschke, and C. Lienau, "Grating-coupling of surface plasmons onto metallic tips: A nanoconfined light source," Nano Lett., vol. 7, no. 9,
- [10] R. F. Oulton, V. J. Sorger, D. A. Genov, D. F. P. Pile, and X. Zhang, "A hybrid plasmonic waveguide for subwavelength confinement and long-range propagation," Nat. Photonics, vol. 2, no. 8, p. 496, 2008.
- [11] P. Biagioni, J.-S. Huang, and B. Hecht, "Nanoantennas for visible and infrared radiation," Rep. Prog. Phys., vol. 75, no. 2, p. 024402,
- [12] F. J. Gonzalez and G. D. Boreman, "Comparison of dipole, bowtie, spiral and log-periodic IR antennas," Infrared Phys. Technol., vol. 46, no. 5, p. 418, 2005.
- [13] F. Neubrech, A. Pucci, T. W. Cornelius, S. Karim, Z. Garcia-Etxarri, and J. Airpurua, "Resonant plasmonic and vibrational coupling in a tailored nanoantenna for infrared detection," Phys. Rev. Lett., vol. 101, no. 15, p. 157403, 2008.
- [14] T. Li, V. Nagal, D. H. Gracias, and J. B. Khurgin, "Sub-wavelength field enhancement in the mid-IR: photonics versus plasmonics versus photonics," Opt. Lett., vol. 43, no. 18, p. 4465, 2018.
- [15] R. Arul, et al., "Giant mid-IR resonant coupling to molecular vibrations in sub-nm gaps of plasmonic multilayer metafilms," Light Sci. Appl., vol. 11, no. 1, p. 281, 2022.
- [16] R. Adato, S. Aksu, and H. Altug, "Engineering mid-infrared nanoantennas for surface enhanced infrared absorption spectroscopy," Mater. Today, vol. 18, no. 8, p. 436, 2015.
- [17] A. C. Jones, R. Olmon, S. E. Skrabalak, B. J. Wiley, Y. N. Xia, and M. B. Raschke, "Mid-IR plasmonics: near-field imaging of coherent plasmon modes of silver nanowires," Nano Lett., vol. 9, no. 7, p. 2553, 2009.
- [18] D. Ji, et al., "Efficient mid-infrared light confinement within sub-5-nm gaps for extreme field enhancement," Adv. Opt. Mater., vol. 5, no. 17, p. 1700223, 2017.
- [19] V. A. Podolskiy and E. E. Narimanov, "Strongly anisotropic waveguide as a nonmagnetic left-handed system," Phys. Rev. B, vol. 71, no. 20, p. 201101(R), 2005.
- [20] A. J. Hoffman, et al., "Negative refraction in semiconductor metamaterials," Nat. Mater., vol. 6, no. 12, p. 946, 2007.
- [21] Z. Jacob, L. V. Alekseyev, and E. Narimanov, "Optical Hyperlens: far-field imaging beyond the diffraction limit," Opt. Express, vol. 14, no. 18, p. 8247, 2006.
- [22] A. Salandrino and N. Engheta, "Far-field subdiffraction optical microscopy using metamaterial crystals: theory and simulations," Phys. Rev. B, vol. 74, no. 7, p. 075103, 2006.
- [23] Z. Liu, H. Lee, Y. Xiong, C. Sun, and X. Zhang, "Far-field optical hyperlens magnifying sub-diffraction-limited objects," Science, vol. 315, no. 5819, p. 1686, 2007.
- [24] J. Sun, T. Xu, and N. M. Litchinitser, "Experimental demonstration of demagnifying hyperlens," Nano Lett., vol. 16, no. 12, p. 7905,
- [25] H. N. S. Krishnamoorthy, Z. Jacob, E. Narimanov, I. Kretzschmar, and V. Menon, "Topological transitions in metamaterials," Science, vol. 336, no. 6078, p. 205, 2012.
- [26] G. V. Naik, J. Liu, A. V. Kildishev, V. M. Shalaev, and A. Boltasseva, "Demonstration of Al:ZnO as a plasmonic component for

- near-infrared metamaterials," Proc. Nat. Acad. Sci., vol. 109, no. 23, p. 8834, 2012.
- [27] Y. C. Chang, et al., "Realization of mid-infrared graphene hyperbolic metamaterials," Nat. Commun., vol. 7, no. 1, p. 10568,
- [28] M. A. K. Othman, C. Guclu, and F. Capolino, "Graphene-based tunable hyperbolic metamaterials and enhanced near-field absorption," Opt. Express, vol. 21, no. 6, p. 7614, 2013.
- [29] K. Korzeb, M. Gajc, and D. A. Pawlak, "Compendium of natural hyperbolic materials," Opt. Express, vol. 23, no. 20, p. 25406, 2015.
- [30] Y. Cui, et al., "Ultrabroadband light absorption by a sawtooth anisotropic metamaterial slab," Nano Lett., vol. 12, no. 3, p. 1443,
- [31] A. Poddubny, I. Iorsh, P. Belov, and Y. Kivshar, "Hyperbolic metamaterials," Nat. Photonics, vol. 7, no. 12, p. 948, 2013.
- [32] A. A. Govyadinov and V. A. Podolskiy, "Metamaterial photonic funnels for subdiffraction light compression and propagation," Phys. Rev. B, vol. 73, no. 15, p. 155108, 2006.
- [33] K. Li, et al., "Subdiffraction limited photonic funneling of light," Adv. Opt. Mater., vol. 8, no. 24, p. 2001321, 2020.
- [34] J. Khurgin, "How to deal with the loss in plasmonics and metamaterials," Nat. Nanotechnol., vol. 10, no. 1, p. 2, 2015.
- [35] L. Nordin, et al., "Enhanced emission from ultra-thin long wavelength infrared superlattices on epitaxial plasmonic materials," Appl. Phys. Lett., vol. 116, no. 2, p. 021102, 2020.
- [36] N. Ahmed and F. A. Inam, "Which plasmonic nano-antenna is best for free-space out-coupling of single photon emission from a hyperbolic metamaterial resonator?," Opt. Lett., vol. 46, no. 9, p. 2212, 2021.
- [37] K. Feng, G. Harden, D. Sivco, and A. J. Hoffman, "Subdiffraction confinement in all-semiconductor hyperbolic metamaterial resonators," ACS Photonics, vol. 4, no. 7, p. 1621, 2017.
- [38] S. Hu, et al., "Experimental realization of deep-subwavelength confinement in dielectric optical resonators," Sci. Adv., vol. 4, no. 8, p. eaat2355, 2018.
- [39] A. Muhowski, E. Simmons, K. Li, E. E. Narimanov, V. A. Podolskiy, and D. Wasserman, "Extending plasmonic response to the

- mid-wave infrared with all-epitaxial composites," Opt. Lett., vol. 47, no. 4, p. 973, 2022.
- [40] C. L. Cortes, W. Newman, S. Molesky, and Z. Jacob, "Quantum nanophotonics using hyperbolic metamaterials," J. Opt., vol. 14, no. 6, p. 063001, 2012.
- [41] V. Drachev, V. A. Podolskiy, and A. Kildishev, "Hyperbolic metamaterials: new physics behind a classical problem," Opt. Exp., vol. 21, no. 12, p. 15048, 2013.
- [42] H. Chen, S. Xu, and J. Li, "Negative reflection of waves at planar interfaces associated with a uniaxial medium," Opt. Lett., vol. 34, no. 21, p. 3283, 2009.
- [43] S. R. Entezar and M. K. Habil, "Refraction and reflection from the interface of anisotropic materials," Phys. Scripta, vol. 94, no. 8, p. 085502, 2019.
- [44] K. G. Balmain, A. Luttgen, and P. Kremer, "Resonance cone formation, reflection, refraction, and focusing in a planar anisotropic metamaterial," IEEE Antenn. Wireless Propag. Lett., vol. 1, p. 146, 2002.
- [45] S. Thongrattanasiri, J. Elser, and V. A. Podolskiy, "Quasi-planar optics: computing light propagation and scattering in planar waveguide arrays," J. Opt. Soc. Am. B, vol. 26, no. 12, p. B102, 2009.
- [46] P. Ginzburg, et al., "Spontaneous emission in non-local materials," Light Sci. Appl., vol. 6, no. 6, p. e16273, 2017.
- [47] J. Elser, V. A. Podolskiy, I. Salakhutdinov, and I. Avrutsky, "Nonlocal effects in effective-medium response of nanolayered metamaterials," Appl. Phys. Lett., vol. 90, no. 19, p. 191109, 2007.
- [48] K. Li, et al., "Ballistic metamaterials," Optica, vol. 7, no. 12, p. 1773,
- [49] COMSOL AB, v. 6.1, 2022. Available at www.comsol.com.
- [50] J. LaMountain and V. A. Podolskiy, "Anomalous reflection in photonic funnels," 2024. Available at: https://github.com/viktorpodolskiy/.

Supplementary Material: This article contains supplementary material (https://doi.org/10.1515/nanoph-2024-0213).